Journal of Alloys and Compounds 896 (2021) 163122

Contents lists available at ScienceDirect

Journal of Alloys and Compounds

journal homepage: www.elsevier.com/locate/jalcom

Review

A review on mechanical properties and microstructure of ultrafine grained metals and alloys processed by rotary swaging

Qingzhong Mao, Yanfang Liu, Yonghao Zhao*

Nano and Heterogeneous Materials Center, School of Materials Science and Engineering, Nanjing University of Science and Technology, Nanjing 210094, China

ARTICLE INFO

Article history:
Received 8 November 2021
Received in revised form 2 December 2021
Accepted 2 December 2021
Available online 4 December 2021

Keywords:
Rotary swaging
Material properties
Microstructure
Ultrafine grain
Severe plastic deformation

ABSTRACT

Rotary swaging (RS), as a widely used industrial method for severe plastic deformation (SPD), is a near net forming process which uses high-speed pulse hammer of multi-hammer to process solid shaft parts or hollow variable cross-section forgings. Initially RS is mainly used to manufacture difficult-to-deform metals with poor plasticity (such as W and Mg alloys, etc.). Recently, because RS process can enable large hydrostatic stresses and facilitate the accumulation of large strain, it is also allowing for high-throughput mass production of different metals with enhanced mechanical properties. This paper first introduces the RS working principle and unique characteristics, then systematically summarized the microstructural characteristics (grain size, texture, etc.), mechanical properties (such as strength, ductility, etc.), physical and chemical properties of various ultrafine grained metals prepared by RS, finally compares the advantages and disadvantages of swaging with other deformation methods, and looks forward to the future development and application fields of rotary swaging.

Contents

* Corresponding author.
E-mail address: yhzhao@njust.edu.cn (Y. Zhao).

https://doi.org/10.1016/j.jallcom.2021.163122
0925-8388/

1. Introduction

As the basic building block of polycrystalline materials (metals, alloys, ceramics, intermetallics, etc.), the grains have a significant effect on the properties and deformation mechanisms of the materials via their size, shape and distribution [1–3]. The relationship between grain size and yield strength of polycrystals was first confirmed by Hall and Petch in the 1950s. For a pure metal, its yield strength is inversely proportional to the square root of grain size [4,5]. As shown in Fig. 1, based on the classical dislocation block model, the grain boundaries (GBs) act as barriers to dislocation motion. And with the grain size decreases, the yield strength of the materials increases rapidly. However, when the grain size is 10–100 nm, the emission source of dislocations is transferred from intragranular to GBs. When the grain size is less than 10 nm, the plastic deformation is mediated by GB motions such as GB migration, GB sliding, and grain rotation [6–8], resulting in an inverse Hall-Petch relationship [9]. Therefore, in order to initially determine material properties, the conventional polycrystalline metallic materials are typically graded into four classes according to grain size: coarse grain (CG, > 10 μm), fine grain (FG, 1–10 μm), ultrafine grain (UFG, 0.1–1 μm), and nano-grain (< 100 nm), as shown in Fig. 1.

The most important influence of grain size reduction is simultaneous increases of the yield strength and toughness which makes it possible to reduce the mass of a structural element for bearing the same load. That is, the UFG materials enable the weight lightening of the components [9]. This feature fits perfectly with the current concept for energy saving and environmental protection. Another advantage of UFG materials in mechanical properties is enhanced fatigue properties due to high density of GBs which impede crack propagation. In addition, the UFG materials often display remarkable resistance to corrosion [10] and wear [11]. Therefore, the UFG materials have a widely industrial applications and scientific research prospects.

In recent decades, severe plastic deformation (SPD) methods, such as high-pressure torsion (HPT) [12], equal channel angular pressing (ECAP) [13], accumulated roll bonding (ARB) [14], etc. have been proposed and employed to fabricate UFG and even NC materials. However, these processes are not suitable for large volume metal preparation, because they are designed for small volume specimens in laboratory. For instance, because of ultrahigh accumulated strain, the HPT technology can easily prepare UFG copper (~250 nm), whereas it has an inherent disadvantage of thinness of products (~1 mm) and limited sample size (< 30 mm) [15]. Another effective strategy to strengthen metals is to introduce twin boundaries, a special kind of low-energy high-angle grain boundary, as a hindrance to dislocation slip whose strengthening effect also follows the Hall-Petch relationship [16–18]. Nano-twinned copper prepared by pulsed electrodeposition technique has ultra-high strength and good conductivity (98% IACS, International Annealed Copper Standard) [18]. Furthermore, the CG FeMnC steel containing gradient hierarchical nanotwins can also break the strength-ductility trade-off [16]. Recently, studies have been refocused on the development of continuous processes based, for example, on rolling and rotary swaging (RS) [19,20]. The preparation of bulk UFG metallic materials by cold rolling combined with appropriate annealing [21] has received a great deal of research. In this brief review, we will focus on mechanical properties and microstructure of UFG metals and alloys processed by rotary swaging.

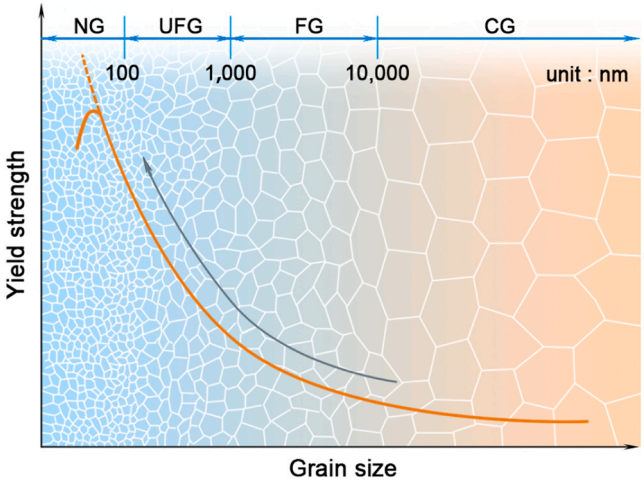

Fig. 1. Yield strength-grain size curve and grain size regimes of CG—coarse grain, FG—fine grain, UFG—ultrafine grain, and NG—nano-grain.

As an industrialized, low-cost, and continuous manufacturing process, RS technology can prepare UFG metals through its unique centrosymmetric stress and strain [22]. In this brief review, we focus on the preparation and microstructure characteristics (grain size, texture, etc.) of UFG metals fabricated by RS and linked properties (such as strength, fatigue, corrosion resistance, etc.), and compares the advantages and disadvantages of swaging with other deformation methods. Finally, we look forward to the future development and application fields of swaging.

2. Rotary swaging

2.1. Theory of rotary swaging

RS is an incremental and chipless metal forming process that reduces the cross-sectional area or changes the shape of solid bars, tubes, wires and other cylindrical parts by repeated radial blows with sets of opposed dies [23], which is schematically depicted in Fig. 2(a). The forging die is evenly arranged around the workpiece of rod bar. When the spindle rotates, it drives the forging hammer and the forging die to rotate together. Due to the centrifugal force, the forging hammer and die are easy to move outward along the diameter. When the forging hammer is located in the middle of the two rollers, the die is opened to the maximum extent. When the top of the forging hammer is facing the roller, the die is closed. Therefore, the forging die move radially with short stroke and high frequency. Finally, under the action of multi-directional forging and high-frequency loading, the rod-shaped billet is uniformly reduced. In order to clarify the microstructure of materials, the orientations and cross-section of the piece are defined in Fig. 2(b). According to the workpiece geometry variations, RS is usually divided into infeed swaging (Fig. 2(c)) and recess swaging (Fig. 2(d)) [24]. The infeed method is often used in the situation where the part is necked through the whole volume, while the recess method is utilized to reduce the diameter at a certain position of the part [25]. In practice, in the case of recess process, the formability of tubes seems to be more attractive than their mechanical properties. Thus, in the following sections, we will focus on reviewing the microstructure and properties of solid metal bars processed by the infeed RS.

The process parameters such as die geometry, feed velocity, rotation speed, percent reduction of one pass and the friction coefficient play a key role in the RS duo to their decisive impact on the workpiece. As shown in Fig. 2(e), unsuitable process parameters often lead to occurrence of defects: (1) fracture; (2) concave head end; (3) spiral ridge; (4) flash; (5) twist [26]. During RS at room temperature, the concave head end is the most likely defect because the deformation in each pass is less than what is needed to achieve forging penetration: $\varepsilon \geq \varepsilon_0$, where ε is the equivalent effect variation in the center of the workpiece, ε_0 is a constant related to the material. When the recrystallization is desired in RS, ε_0 is the critical strain of the material undergoing dynamic recrystallization [27]. Although these process parameters affect the microstructures and properties of the RSed materials, the most critical factor is the strain accumulated in the RS. The equivalent strain is

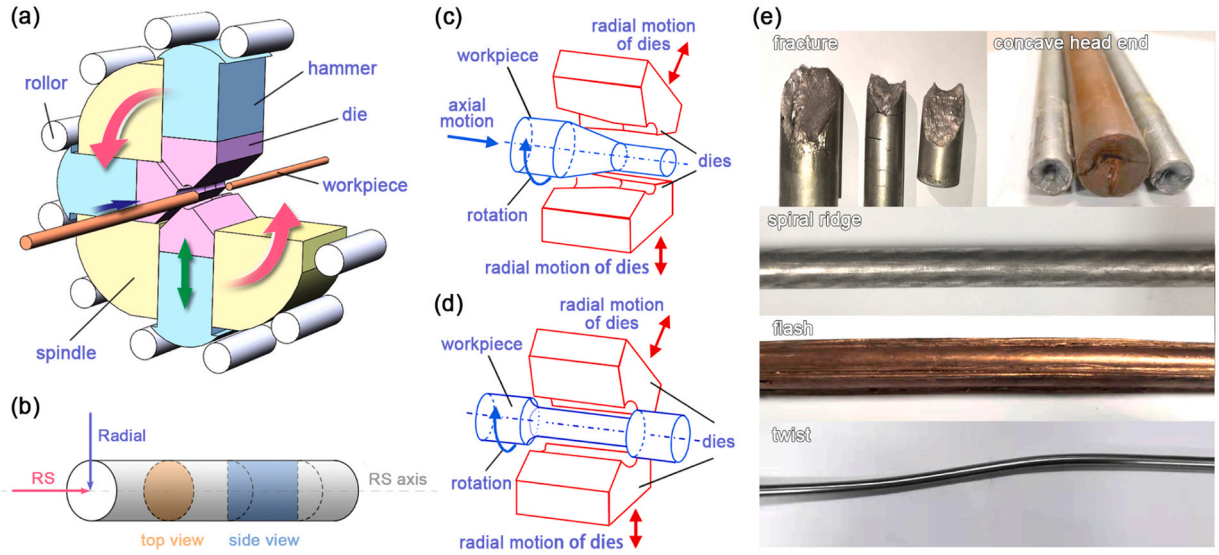

Fig. 2. Schematic diagram of (a) the rotary swaging (RS) principle and (b) the principal observations of the microstructure [22], (c) the infeed process and (d) the recess press [24]; (e) processing defects in rotary swaging.
Reproduced with permission from Refs. [22,24].

defined as $\varphi = ln(A_0/A)$ where A_0 and A are the initial and final cross-section area of the solid bar, respectively [28,29]. Similar other SPD processes, a high equivalent variation in RS leads to a high strength until equilibrium is reached.

In practice, centrosymmetric compressive force is loaded onto the encircle workpiece through simultaneous radial movements of forming dies, and thus, there is a mixed stress of 2-axial compression and uniaxial tension applied to the RSed materials [30]. In addition, the friction between the workpiece and the dies also causes shearing action along the die rotation direction. Fig. 3 shows the macrographs of homogeneous Cu alloy and Cu-Al clad composite (the light is Cu and the dark is Al) after RS at room temperature. It is obvious that the radial grains were stretched out along the RS axis of the rod (middle subgraph in Fig. 3(a)), and from top view, the grains are arranged in a spiral pattern under shear stress (right subgraph in Fig. 3(a)). A similar spiral arrangement is found in RSed Cu-Al clad composite which is deformed from Ø30 mm to Ø5 mm (with strain of 3.6) with the cross-sectional shrinkage of 97% and the axial elongation of 3600%. In contrast, the shearing effect of workpiece during RS seems to be negligible. Moreover, this effect can be reduced by reducing the friction coefficient and increasing the deformation temperature.

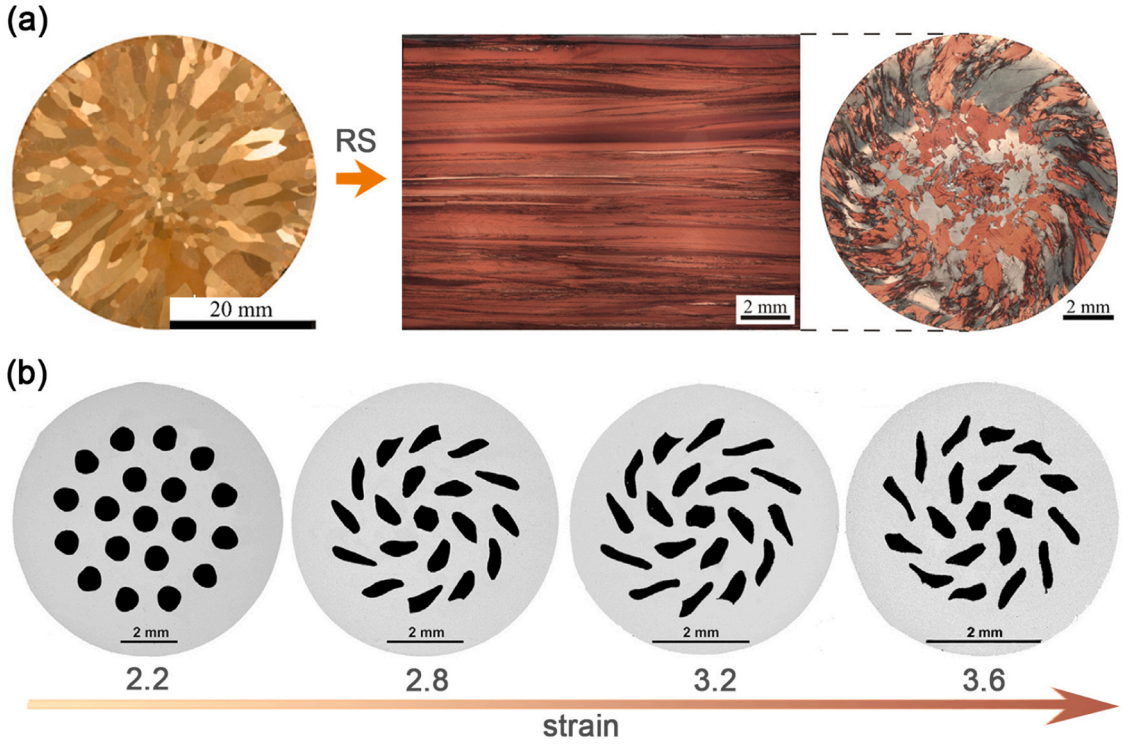

Fig. 3. Macrographs of (a) Cu-0.008 wt% Bi before and after rotary swaging (RS), the circles are top view and the rectangle is side view [31], (b) top view of swaged Cu-Al clad composite with various equivalent strain [32]. All deformed at room temperature.
Reproduced with permission from Refs. [31,32].

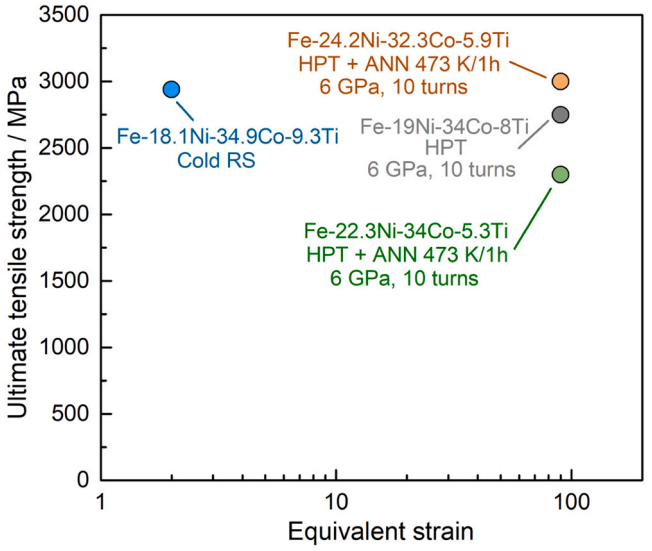

Fig. 4. Effect of equivalent strain by rotary swaging (RS) and high pressure torsion (HPT) on ultimate tensile strength in Fe-Ni-Co-Ti alloys [33].
Reproduced with permission from Ref. [33].

It is well known that metals can be significantly strengthened by UFG/NC microstructures which could be prepared by the SPD methods via accumulation of strain. In principle, ECAP and HPT are capable of infinite accumulative strain without volume change, so a great deal of interest has been focused on them. As a deformation process with reduction of diameter, accumulated strain of RS is usually less than 4. Industrially, RS is mainly used for (1) tube forming, connection and dimensional stability; (2) reducing porosity in sintered powders; (3) difficult to deform and less plastic metals (such as W and Mg alloys, etc.). Therefore, the preparation of UFG or even NG structure by RS has not received much attention. Fortunately, due to its unique stress state, RS can strengthen materials with very high efficiency. Fig. 4 shows the effect of equivalent strain of Fe-Ni-Co-Ti alloys during the RS and HPT processes on the ultimate tensile strength. The RSed alloy with strain of 2 reaches as much as 3 GPa of ultimate tensile strength (UTS) and is comparable in strength to HPTed alloy with strain of 90 [33]. Even if the strain is only equal to 2–3, the RSed metal can still has a UFG/NC structure which will be discussed in Section 3.1.

2.2. Residual stress in rotary swaged metals

Generally, residual stress is the stress that remains within the material even when unloaded and can be categorized in three types: (1) Type I or macro-stress which acts over a length comparable to the macroscopic dimension of the component; (2) Type II is localized in a length scale comparable to the grain size, and (3) Type III occurs in a length scale smaller than the grain size (for example stress fields around dislocations or at interfaces) [34,35]. Residual stresses can be measured by different methods including X-Ray diffraction (XRD), neutron diffraction, hole drilling, deep hole drilling and the hole contour method as well as block removal [25,35,36].

Quenching, local heating treatment as well as uneven stress can introduce residual stresses to materials. As reported by previous literature, there are significant Type I and Type II residual stresses existed in the RSed material because of inhomogeneous deformation [25,35,36]. In RSed single-phase materials, thanks to the homogeneity of the microstructure, residual stresses are mainly reflected in Type I. While Type I and Type II are obvious in RSed multiphase materials due to strength difference between each phase. The presence of residual stress generally changes the size and shape of the workpiece, and deteriorates the overall performance of the component [34]. However, residual stress does not only play a negative role, it can be controlled to improve the fatigue strength and wear resistance of the part which will be discussed in Section 3.2.2.

Reviewing the previous literature on residual stresses in RSed materials, we found that their properties are controversial, although there is a consensus among all researchers that residual stresses are distributed along a gradient with higher values at the center and smaller values at the edges. Canelo-Yubero et al. used neutron diffraction technique to investigate the residual stresses in tungsten heavy alloy bars prepared by RS at room temperature and 900 °C, and found that the compressive residual stress at the center and the tensile residual stress at the surface in the radial direction of the rod [35]. As a comparison, Singh et al. obtained the exact opposite result in RSed Zr-4 alloy by hole drilling method [25]. Of cause, this phenomenon may be related to the process parameters or the nature of the RSed materials, but based on the current study, we can not draw a definite conclusion.

Another question worth exploring is whether the center has a higher metal flow, that is, whether the center has a high strain compared to the edge during RS. Otto et al. annealed the RSed Cu-Bi bar (Fig. 3(a)) and observed that the microstructure in the core recrystallized first, thus inferring that the center was a strongly deformed region owning to the high strain lowered the threshold for recrystallization [31]. It has also been found that the center of the RSed

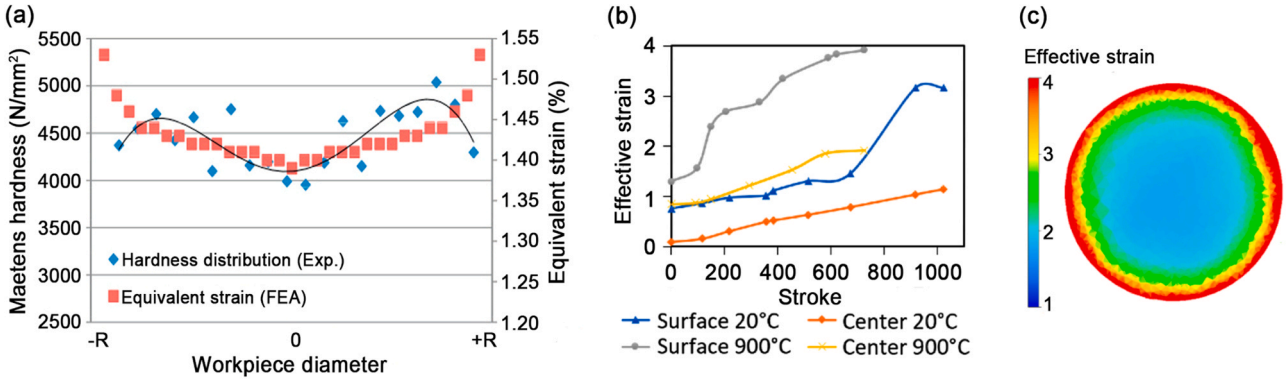

Fig. 5. (a) Hardness (experimental) and strain (finite element analysis, FEA) distribution of steel after a single RS forming [41], (b) development of effective strain in edge and center regions of RSed workpiece at room temperature and 900 °C and (c) effective strain across top-view of warm-swaged tungsten heavy alloy [42].
Reproduced with permission from Refs. [41,42].

rods has higher hardness, thus, it is speculated that this is due to higher metal flow [25,37]. However, observing Fig. 3(a) (right subgraph) and Fig. 3(b) (right subgraph) carefully, each distortion in the center of the RSed rod is obviously lower than that in the edge. Moreover, the strain distribution can be verified by the finite element analysis (FEA). Fig. 5(a) shows the hardness (experimental) and strain (FEA) distribution of steel after one RS pass at room temperature. The distribution of hardness and that of equivalent strain coincide well, simultaneously, they are gradient and distributed along the radial. Because of the lack of constraint, the edge region is more flow, so it has a higher equivalent effect variation. As the RS progresses, the hammers continuously apply load radially on the surface of the workpiece. Fig. 5(b) gives the development of effective strain in edge and center regions of RSed workpiece throughout the deformation process with at least 700 hammer blows. The equivalent strain at the edges is always greater than that at the center, and the high temperature exacerbates their difference. In addition, Fig. 5(c) shows the distribution of the effective strain across the cross-section (top view) through the workpiece swaged at 900 °C. The effective strain of the edge region reaches a value of ~4, and then, gradually decreased towards the center where it reaches the values of ~2. In summary, the center region of the RSed rod should have less flow, but it is objective for the center to have higher hardness/strength in some cases. Mao et al. analyzed the microstructure and mechanical properties of RSed Cu rod in detail and concluded that the high hardness/strength of the center is a result of texture and dislocation density [38,39]. Moreover, the low strain leading to preferential recrystallization is also attributed to the net driving pressure associated with dislocation density [40].

2.3. Advantages and disadvantages of rotary swaging

Compared with other SPD methods, the RS technique offers several advantages, as follow:

- Most importantly, owning to outstanding deformation enhancement and grain refinement abilities, the RS enables deformed metals with small strain are comparable in strength to other SPDed metals with large strain;
- RS allows a gradient stress/strain distribution along the radial direction throughout the workpiece which provides a new opportunity for the preparation of gradient microstructures;
- RS is an industrial, low cost and continuous net-shape-forming process;
- Extra-long wires can be achieved via connecting multiple RS machine in series;
- A modified RS equipment can prepare rod/tube with variable diameter and various cross-sections;
- Wide deformation temperature interval from cryogenic to elevated temperature.

The large disadvantage of RS is the “accumulated strain”. As a deformation method of progressively reduced diameter, the RS is unable to accumulate very high strain. For example, even with cross-section shrinkage of 95%, the strain of RSed rod is just under 3. By contrast, it is very easy to obtain strains over 100 via ECAP and HPT. Therefore, the RS is not suitable for the preparation of some materials requiring ultra-high strain. Another disadvantage is the complex construction of RS equipment which had a high degree of specialization. However, it can be overcome by adding machines.

3. Microstructures and properties of rotary swaged metals

3.1. Microstructures of rotary swaged metals

The RS has proven to be an effective method for the preparation of UFG metals. Metals with different crystal structures tend behave differently under the complex stresses of RS, and then different microstructures will be introduced. Thus, this subsection we discuss the microstructures of three crystal types of metals including face-centered cubic (FCC), hexagonal close-packed (HCP) and body-centered cubic (BCC).

Generally, the FCC metals have the best plasticity because of adequate slip systems that can be activated. Take Cu as an example, the microstructures of initial CG Cu and RSed Cu are shown in Fig. 6(a)–(c) [38]. The annealed Cu is compared of equiaxed grains with a size of ~54 μm and a large number of annealing twins, as well as a random orientation (Fig. 6(a)). After the RS with a stain of 2.5 at room temperature, the grains are significantly refined and elongated with an average length of 300 μm in the axial direction and a width of 2 μm in the radial direction, where dislocation cells with a length of 25 μm and a width of 220 nm inside (Fig. 6(b) and (c)). For pure Cu with a typical medium stacking fault energy, the dislocation substructures such as dislocation cells, dense dislocation walls and lamellar sub-grains are the characteristic microstructures observed during the microstructural evolution process [43]. In addition, the RS process gradually introduces strong < 111 > and < 100 > fiber textures parallel to the axial direction. Comparing the microstructures of the center and the edge of the RSed Cu rod, we can find that the difference is mainly in the dislocation density and fiber texture distribution, but not in the grain size. In typical FCC metals, Al [29] and Ni [44], because it is difficult to reach the critical strain of the material undergoing dynamic recrystallization, such grains with high aspect ratios are common after RS at room temperature. However, this deformed microstructure can significantly reduce the plasticity of the FCC metals. In order to obtain equiaxed UFG structure, a complex thermo-mechanical treatment including conventional solution treatment, peak-aging, RS and re-aging was developed. Huang et al. used this method to prepare a UFG CuCrZr alloy (with a strain of 2.6) which has a high performance of an UTS of 612 MPa, a uniform elongation of 5% and an electrical conductivity of 84.7% IACS [45]. The UFG microstructure is shown in Fig. 6(d), partial grains recovery and recrystallization duo to heating, and overall, a few dislocations in the grains which with a size of ~400 nm.

According to the Von-Mises criterion, at least 5 independent slip systems are required for polycrystals to achieve uniform plastic deformation by individual dislocation slip [46]. However, there are only 4 independent slip system in the HCP system, so it is necessary to open the < c+a > pyramidal slip or twinning to coordinate the deformation, otherwise the HCP metals will have a very poor plasticly [47]. It has been proofed that the < c+a > slip and twinning are sensitive to grain size [48–50]. The deformation twinning propensity in UFG Ti decreases monotonously and transforms to < c > slip with decreasing grain size [50]. K. Wei et al. reported that the reduction of grain size can induce the activation of < c+a > dislocations which helps to accommodate strain along c -axis and improves the uniform elongation of pure Mg [48]. In practice, the c/a ratio directly affects the type of slip that can be activated in the HCP metals. Generally, Ti has a good plasticity, that is due to its axial ratio is 1.587 which is obviously less than the ideal value of 1.633. By RS and subsequent annealing, Wang et al. prepared UFG commercially pure Ti (grade 2, with strain of 2.77), as shown in Fig. 7(a) (side view) and (b) (top view) [51]. Obviously, the grains are not completely recrystallized. The microstructure after RS is still retained (side view), because the grains are similar to the RSed FCC structure from the side view which are elongated in the axial direction (Fig. 6(b) and (c)), however, from the top view, recrystallized grains (~1 μm) and very small sub-grains (200–400 nm) are observed. In the case of Mg alloys, it has an axial ratio of 1.624 which is very close to the value of ideal HCP structure, so most of Mg and its alloys show poor plasticity or formability. The ways to improve their plasticity are to activate the < c+a > pyramidal slip and to introduce twins. Fortunately, the special stress state of RS plays an important role in activating < c

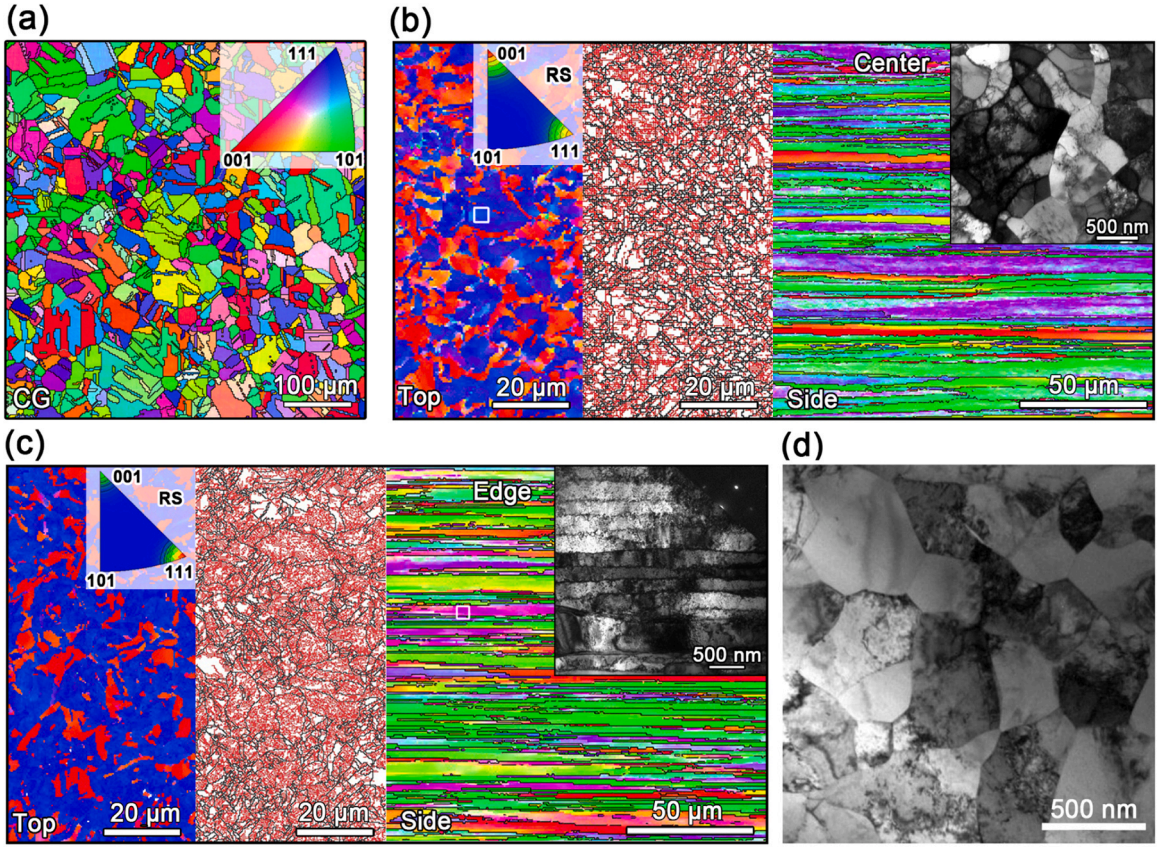

Fig. 6. Crystal orientation maps and grain boundary maps of (a) coarse grain (CG) in copper before rotary swaging (RS), the inset is color code in which red, green and blue indicate grains having < 001 > , < 101 > and < 111 > directions perpendicular to the paper, respectively; (b) the center region and (c) the edge region of RSed rod with a strain of 2.5 at room temperature, the insets in the upper right are Inverse pole figures of axil direction, and the insets in the upper right are the transmission electron microscopy (TEM) image corresponding regions marked by white square [38]. (d) TEM image of CuCrZr alloys treated with solution treatment + peak-aging + RS + re-aging [45].
Reproduced with permission from Refs. [38,45].

+a > pyramidal slip and twinning in Mg alloys [52,53]. The refinement mechanism of Mg alloys during RS was well investigated in three main stages: (1) in the early stage of RS, a large number of deformation twins are introduced, (2) with increasing of strain, initial grains fragment into many small grains or sub-grains, (3) a completely homogeneous microstructure with equiaxed UFG is formed [54,55].

Interestingly, except for the UFG microstructure, Chen et al. realized the preparation of gradient structure in AZ31B Mg alloy using the gradient strain/stress in RS [54]. Fig. 7(c)–(f) shows the microstructures of the RSed AZ31B with a strain of 0.24 in different regions along the radial direction. There exists an obvious gradient distribution of grain size. The edge region (with 6.5 mm distance to the center) exhibits many twin lamellae with a width of ~300 nm (Fig. 7(c)). The transition region (with 4 mm distance to the center) consists an inhomogeneous microstructure containing mostly twin lamellae (marked by "T") and UFGs as well as a small quantity of NGs (Fig. 7(d)). The transition region (with 2 mm to the center) exhibits another inhomogeneous microstructure with NGs and UFGs (Fig. 7(e)). The center region has a completely homogeneous microstructure with equiaxed NGs with an average size of ~93 nm (Fig. 7(f)).

In this part, we transfer the gaze to the RS deformation of BCC metals, such as W and Fe. Tungsten heavy alloys (THAs) are usually prepared from powder mixtures consisting of > 90 wt% of W particles and elements with lower melting points (Ni, Co, Fe) dissolving between W particles during sintering [56]. Due to its incremental character and favorable stress state, the RS can effectively reduce the porosity in the sintered powder [57,58]. Fig. 8(a) and (b) shows the microstructure (side view) of the cold RSed 90%W-7%Ni-3%Fi alloy with strain of 0.7 and 1.7, respectively. With the increase of strain, the initial round W particles (light region) were elongated along the axial direction under the applied load. However, the aspect ratio of the deformed W particles is significantly smaller compared to that of swaged pure Cu grains. This occurs because the harder W particles are encapsulated by the softer binder which enhancing the coordination between them. Typically, hot RS is substituted for cold RS to reduce the risk of cracking of THAs during the forming process. Fig. 8(c) shows the microstructure (side view) of a hot RSed WNiCo alloy with strain of 0.36. In fact, the structure of top view and that of side view are similar, the W particles are slightly flattened. In general, high temperature can also lead to an increase in flow of THAs. It should be noted that according to the previous literature, we did not find any UFG THAs prepared by RS method. Another BCC metal—UFG Fe, however, can be fabricated by hot RS. A CG Fe-Al_2O_3 alloy was hot RSed at 960 ℃, and the grain microstructure is considerably elongated (the width of grains 200 nm, aspect ratio 2.2) in the direction of swaging axis, as shown in Fig. 8(d). In summary, the SPD-induced grain refinement process for BCC metals is somehow similar to that observed in FCC metals: Stage I, individual grains are quickly subdivided into many volume elements delineated by dense dislocation walls; Stage II, significant amounts of dislocations accumulate at cell walls and dense dislocation walls, as a result of higher misorientation; Stage III, large amounts of lamellar sub-grains enclosed by lamellar boundaries form, resulting in continuous reduction of cell block sizes and significant increase of misorientation; Stage IV, lamellar structures become finer and clearly some equiaxed grains start to form; Stage V, overall grain refinement reaches a steady state [43].

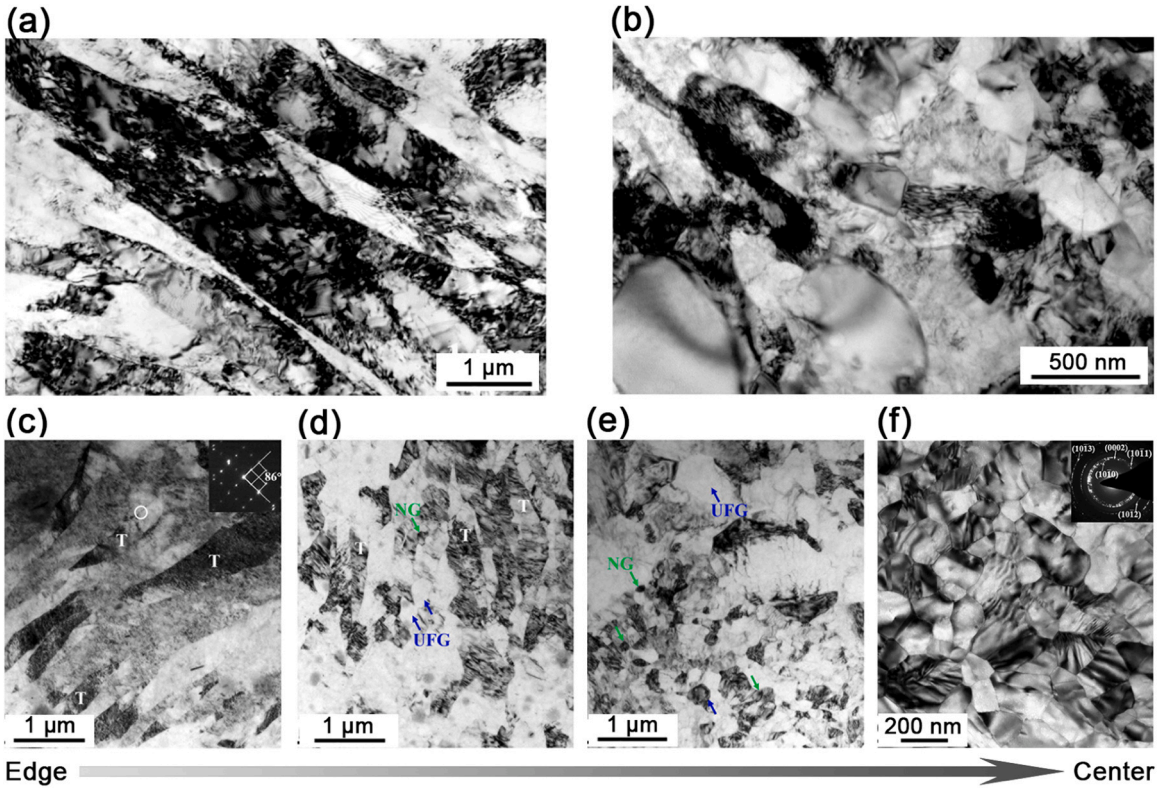

Fig. 7. Typical TEM images of (a) side view and (b) top view of commercially pure Ti treated with rotary swaging (RS) + annealing [51]; (c–f) microstructures in the transition region of AZ31B Mg alloy with a distance to the center of approximately 6.5 mm, 4 mm, 2 mm and 0 mm, respectively [54]. NG: nano-grain; UFG: ultrafine grain; T: twin. Reproduced with permission from Refs. [51,54].

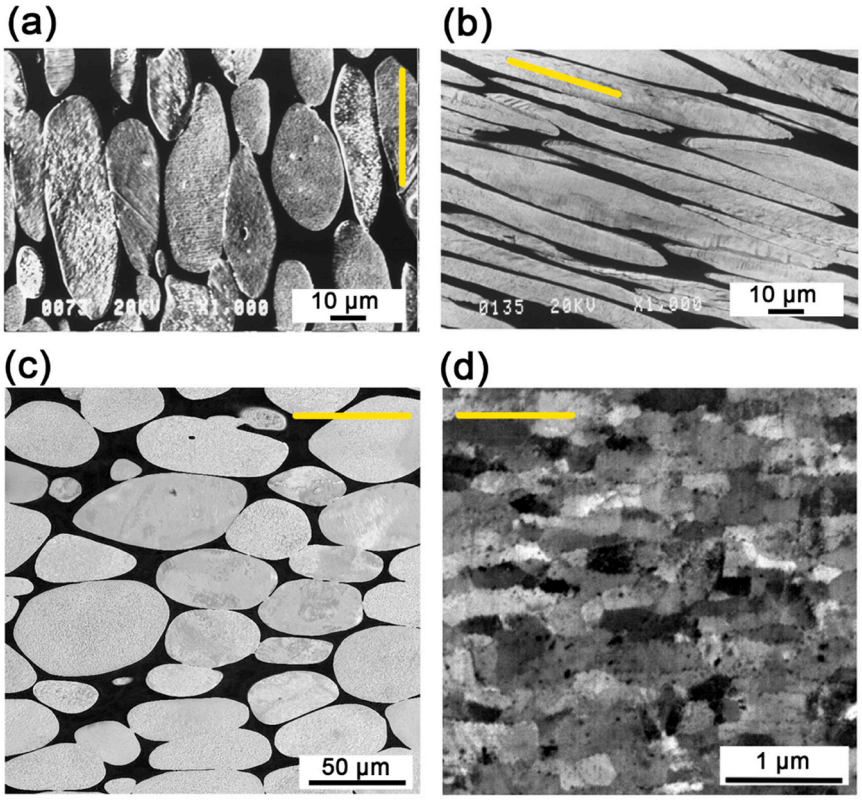

Fig. 8. Microstructures in side view of the cold RSed WNiFe alloy with (a) strains of 0.7 and (b) 1.7 [57], (c) the hot RSed WNiCo alloy with a strain of 0.36 [56], (d) the hot RSed Fe-Al_2O_3 alloy with a strain of 2.4 [59]. Yellow lines indicate axial direction.
Reproduced with permission from Refs. [56,59].

Table 1
Tensile properties, hardness and grain size of various metals before and after rotary swaging (RS).

Materials	Process	Strain	GS*/μm	HD*/HV	YS*/MPa	UTS*/MPa	EL*/%	Ref.
Al 1050	CG*	–	450	24	20	72	120 (F*)	[60,61]
	RS*	3	0.75	49	158	163	11.6 (F)	
AA 5083	CG	–	25	91	180	340	17.2 (U*)	[62]
	RS	2	2	148	430	460	2.8 (U)	
316L	CG	–	35	–	454	696	55.1 (F)	[63]
	RS	1.65	3	–	647	736	35.3 (F)	
CrMnNi	CG	–	28.1	–	365	832	59 (U)	[64]
	RS+ANN*	2.4	0.7	–	923	1063	21 (U)	
CuCrZr	CG	–	–	–	284	350	9.9 (U)	[45]
	RS+ANN	2.6	~0.4	–	590	612	4.6 (U)	
Ni	CG	–	–	–	148	462	46 (F)	[44]
	RS	1.7	1	250	753	763	14 (F)	
L-Steel*	CG	–	10	–	460	600	27 (F)	[65]
	Hot RS	2.3	0.33	–	922	927	14.5 (F)	
CP* Ti	CG	–	90	118	155	370	57 (F)	[66]
	RS	2.7	0.1	236	875	920	11 (F)	
	RS+ANN	2.7	0.36	178	585	745	18 (F)	
VT8M-1	CG	–	3	–	970	1040	5 (U)	[67]
	RS	1.7	0.25	–	1150	1230	3.8 (U)	
WE43	CG	–	70	–	150	220	10.2 (F)	[68]
	Hot RS	1	0.61	–	285	415	7 (F)	
MgGdYZr	CG	–	8	–	200	320	14 (U)	[53]
	RS	0.43	0.08	–	560	630	3 (U)	
	RS+Aging	0.43	0.08	–	650	710	4 (U)	

* GS: grain size, for not equiaxed grains, the values given are the grain widths; HD: hardness; YS: yield strength; UTS: ultimate tensile strength; EL: elongation, F means elongation to fracture and U means uniform elongation, respectively; CP: commercially pure; L-Steel: Low-Steel; CG: coarse grain; RS: rotary swaging; ANN: annealing.

3.2. Properties of rotary swaged metals

3.2.1. Hardness and strength

It is well known that high hardness in metallic materials leads to high strength, and Mao et al. has established it in RSed Cu via hardness and single-axis tensile tests [38]. Table 1 lists the CG metals and corresponding UFG structures prepared by RS or RS + heat treatment as the final process and their corresponding properties. Because of the similar properties, we also listed the results for NG and some FG (several micrometers) materials as well. Based on the results in Table 1, we can find that (1) as compared with other SPD methods, cold RS can significantly increase the strength of CG metals which is accompanied with the sacrifice of ductility; (2) RS can efficiently prepare UFG or NG metals although the equivalent strain is small; (3) hot RS or clod RS + heat treatment can fabricate UFG metals with excellent strength-ductility combination.

According to the past literature, there is an interesting phenomenon that the hardness/strength distributions on the cross-section (top view) of the RSed metals are not definite. It can be roughly summarized into three categories: (1) type I, the hardness of center is higher than the edge and gradually decreases along the radial direction (CoCrFeMnNi alloy in Fig. 9(a)); (2) type II, the hardness distribution is relatively uniform on the radial direction (MA 956 alloy in Fig. 9(a)); (3) type III, contrary to type I, the hardness of edge is higher than that of the center (WNiCo alloy in Fig. 9(a)). Among them, the type I is the most frequent case [28,38], and the type III is mainly found in W alloys [56,69], while type II is relatively rare [70]. For type I, some researchers believe that the higher hardness in the RSed metals is caused by higher strain, however, it may be incorrect according to the discussion in Section 2.2, since the edge region has higher strain. Then, Chen et al. and Mao et al. explained this phenomenon in terms of microstructure [38,54]. Chen et al. suggested that the gradient distribution in RSed AZ31B Mg alloy is due to the gradient grain size which has been shown in Fig. 7(c)-(f). The RS process of pure Cu rod was studied in detail by Mao et al., and they found that the distribution of hardness developed with strain. As shown in Fig. 9(b), all three hardness distributions are found in the RSed Cu. At the beginning stage of deformation with a strain of 0.08, the micro hardness distribution is type III. The higher microhardness at the edge is because more deformation occurred first at the edge and has not been delivered to the center yet due to (1) the direct contact of Cu rod surface and swaging dies, (2) the resistance and hysteresis of Cu to the deformation. When the strain is equal to 0.25, the hardness of the center and the edge are equal (type II appears). And then, as the strain increases, the center hardness starts to be higher than the edge and remains (type I). Therefore, which hardness distribution appears is determined by the corresponding strain. In the case of W alloys, we found that the hardness distribution in both cold and hot RS is type III. However, the hardness distribution of RSed Nb, also a typical BCC metal, is type I [71]. It indicates that the hardness distribution in W alloys is caused by its special microstructure, where the soft phase wraps around the hard phase, and the enhanced coordination prevents the center from accumulating sufficient strain to strengthen.

Below we discuss the higher strength in the center of RSed Cu with a strain of 2.5. Due to the application of multidirectional loads, the center of the rod is a difficult relaxation region (inset in Fig. 9(b)). Thus, different from the microstructure of the edge, the center region has more < 111 > fiber texture and dislocations which are statistics in Fig. 9(c). This difference in dislocation density and texture can also be seen when comparing Fig. 6(b) and (c). The yield stress (σ_y) of the swaged copper can be estimated comprehensively by the following equation [39,72]:

$$\sigma_y = \sigma_{GB} + \sigma_0 + \sigma_{dis} = \sigma_{GB} + M\tau_0 + M\tau_{dis}$$

where σ_{GB} is grain boundary strengthening contribution, M is average Taylor factor which is determined by the texture, τ_0 is the intrinsic critical resolved shear stress which is a constant, and τ_{dis} is dislocation strengthening contribution which is determined by the density of dislocation. Fig. 9(d) shows the experimental yield strength and the strength calculated based on Fig. 9(c) of the center and the edge, respectively. It can be found that the calculated results match well with the experiment. Since the same grain size was observed in the center and the edge of the RSed Cu (Fig. 6(b) and (c)), they have the same σ_{GB}. Therefore, the higher M and dislocation

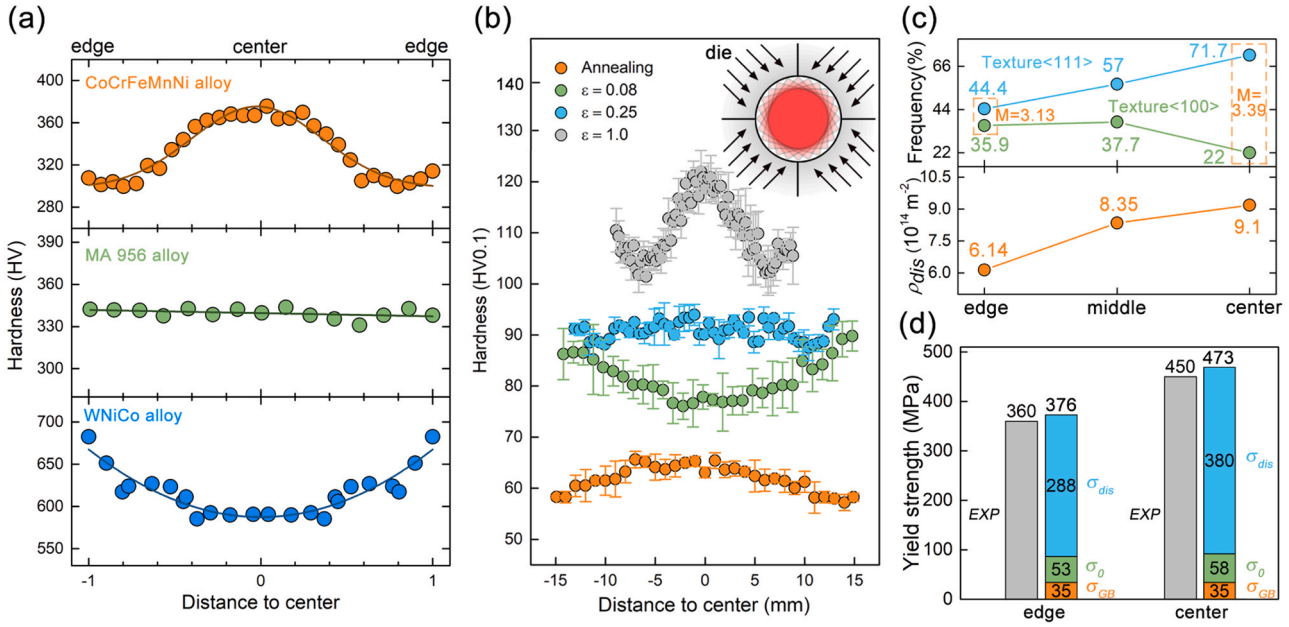

Fig. 9. (a) Three typical hardness distribution trends in RSed metals (top view) [56,70,73], the "Distance to center" has been normalized, 0 indicates the center and 1 indicates the edge; (b) hardness distribution in RSed pure Cu with different strains, the inset is schematic representation of the loading superposition, (c) fiber texture and density of dislocation distributions in RSed pure Cu with a strain of 2.5, (d) experimental and calculated yield strength based on (c) [38]. M: Taylor factor; σ_{dis}: density of dislocation; σ_0: intrinsic strengthening contribution; σ_{GB}: grain boundary strengthening contribution; EXP: experimental result.
Reproduced with permission from Refs. [38,56,70,73].

density of the center leads to its higher yield strength. In addition, the preferential occurrence of recrystallization in many metals during annealing is also due to the net driving pressure associated with dislocation density [40].

3.2.2. Fatigue

Unlike static damage by uniaxial tensile, fatigue fracture is a process of accumulation of damage [60,66]. Even if the applied cyclic stress is much less than the UTS of the material, when the number of cycles reaches a certain number, the material may fracture [64]. Therefore, it is necessary to test the fatigue performance of the material according to the service environment requirements. There are two main indicators to assess the fatigue performance of a material: fatigue life and fatigue notch sensitivity.

The fatigue performance of the crack formation stage of high cycle fatigue (HCF) is often characterized by the S-N curve, where S is the stress level and N is the fatigue life. In order to investigate the HCF properties of UFG metals prepared by RS, Abdulstaar et al. fabricated a series of Al 1050 with different grain size (0.7, 35 and 450 μm) via cold RS + annealing [60]. Fig. 10(a) shows the S-N curve of three samples without notch, it is clear that the UFG Al has an outstanding fatigue life. The fatigue limit of UFG Al (0.7 μm) is about 125% higher than that of CG Al (450 μm). Generally, the increase in the life of HCF is attributed to residual stress and work hardening [74].

The fatigue performance of the material is also influenced by its fatigue notch sensitivity, because the fatigue performance of notched bodies might be very poor even if the fatigue performance of smooth bodies is good. Fig. 10(b)–(d) compared the fatigue performance of three samples with/without notch. As compared with other SPDed metals, the UFG Al prepared by RS is highly notch sensitive due to low work hardening capability.

The fatigue results concerning RSed metals are consistent in that RS improves the fatigue strength of the metals while strengthening it, but also leads to high notch sensitivity of the material. Reducing the notch sensitivity of RSed metals can be achieved by subsequently annealing to increase the strain hardening coefficient capability of metals, but with the consequent reduction in fatigue resistance [51,60,66].

Therefore, the microstructure with an outstanding fatigue strength-notch sensitivity equilibrium needs to be determined according to suitable process.

3.2.3. Impact toughness

The next mechanical property to be discussed is impact toughness which refers to the ability of the material to absorb plastic deformation work and fracture work under the action of impact load [67].

Fig. 11(a) illustrates the structure and impact toughness of FG and UFG VT8M-1 alloy. Before RS, the microstructure consists of 0.12 μm thick α-phase lamellae divided by β-phase interlayers, and 25% of the globular primary α-phase with an average grains size of 2.7 μm (top subgraph). After RS, the average size of grains and subgrains in the (α + β) areas was 0.25 μm (bottom subgraph). The impact toughness of UFG sample is only 50% of the FG sample, and it shows that the RS process reduces the impact toughness while increasing the strength of the metals. Modina et al. suggested that the fracture mechanism from dimple to intercrystalline is the trigger for the reduction of impact toughness [67]. However, Mao et al. found that the fibrous grains can improve the impact toughness of pure Cu, the structure has been shown in Fig. 6(b) and (c). The authors tested the impact toughness of a series of pure Cu rods with various strains. The impact absorbing energy of RSed Cu increases with increasing strain until equilibrium is reached, as shown in Fig. 11(b). The improvement in impact toughness is mainly attributed to the energy consumption including (1) main crack extension in a zigzag way; (2) fiber grains delamination; (3) small amount of recrystallization at the crack tip (Fig. 11(c)). In addition, due to the super-large grain aspect ratio, the impact absorbed energy of the RSed Cu along axis is believed much smaller than that along radial direction [38]. In literature, a similar ultrafine elongated grain microstructure in low alloy steel was reported to have an enhanced impact absorbing energy (226 J) than its CG counterpart (14 J) [75].

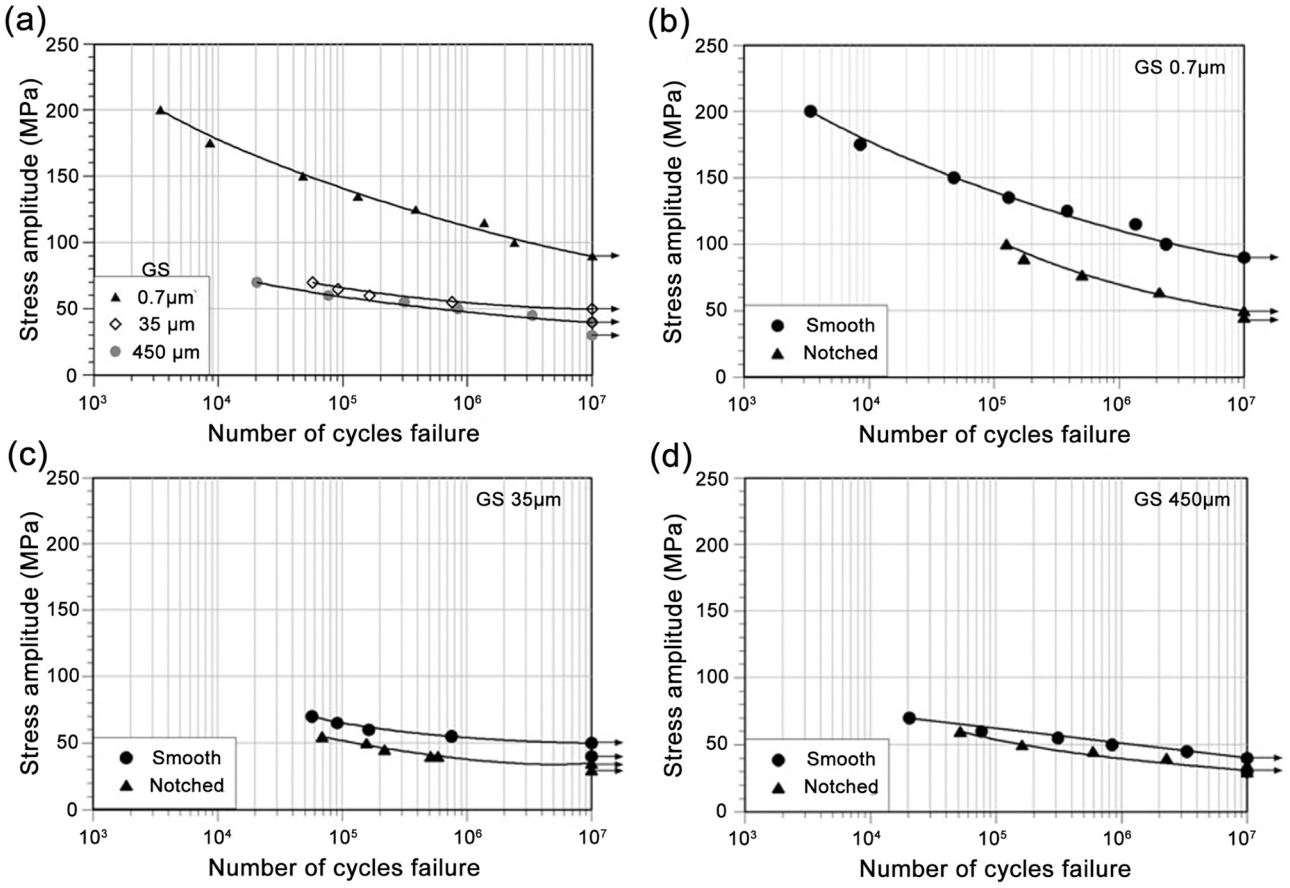

Fig. 10. S-N curves of (a) smooth samples of Al 1050 in rotating bean loading (R = −1) and (b–d) smooth and notched Al 1050 with three GSs in rotating beam loading (R = −1). GS means grain size [60].
Reproduced with permission from Ref. [60].

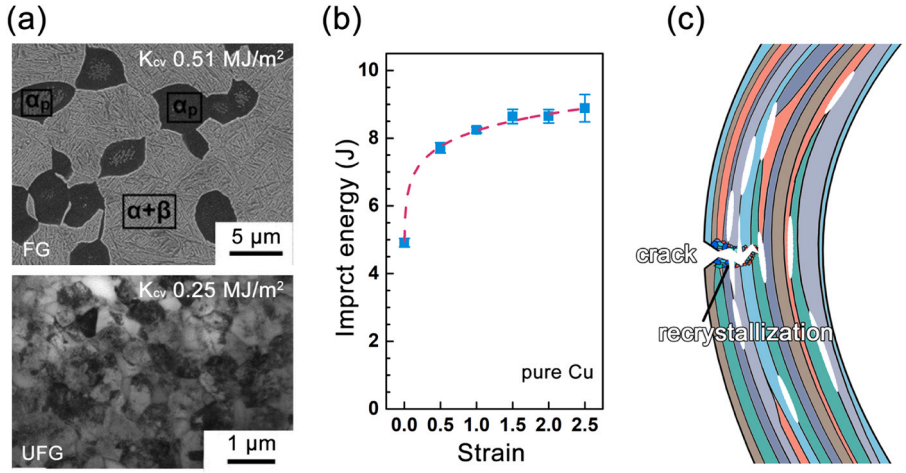

Fig. 11. (a) Microstructures of the VT8M-1 alloy before and after rotary swaging [67]. (b) Charpy absorbed impact energy vs swaging strain curve of pure Cu and (c) Schematic representation of isolate micro cracks and zigzag propagation in swaged Cu under Charpy impact [38]. FG: fine grain; UFG: ultra-fine grain; K_{CV}: impact toughness.
Reproduced with permission from Refs. [38,67].

Therefore, the impact toughness of metals is greatly influenced by their microstructure, and the increasing of the pathway of energy consumption can significantly improve the impact toughness of metals.

3.2.4. Corrosion

The ability of materials to resist the corrosive and destructive effects of the surrounding medium is called corrosion resistance which is determined by the properties of the materials themselves and the corrosive environment together. The potentiodynamic polarization curve, an electrochemical method, is used to evaluate the corrosion behavior of materials in defined solutions. The measured electrochemical characteristics of RSed metals with UFG/FG and corresponding CG counterpart in various structural states are listed in Table 2. Among them, the corrosion potential (E_{corr}) and corrosion current density (I_{corr}) are the most important indicators for

Table 2
Electrochemical characteristics of RSed metals in various structural states.

Materials	Strain	GS* (μm)	E_{corr}* (mV)	I_{corr}* (μA/cm^2)	R_{corr}* (mpy)	Environment	Ref.
Pure Cu	0	71	-214	3.2	–	Hank's solution	[76]
	0.5	54	-198	3.6	–	37 ± 1 °C	
	1	16	-210	4.5	–		
	2	1	-217	3.1	–		
	3	0.2–0.8	-217	2.3	–		
Al 1050	0	450	-716	1.055	0.451	3.5% NaCl solution	[61]
	2	0.76	-708	0.379	0.162	Room temperature	
	3	0.75	-720	0.283	0.154		
AA 5083	0	25	-881	0.369	0.159	3.5% NaCl solution	[62]
	2	2–3	-823	0.145	0.063	Room temperature	
AISI 316	0	35	-541	4.2	0.89	Ringer's solution*	[63]
	1.64	3	-407	2.1	0.731	37 ± 1 °C	
AISI 304	0	36.4	-390.5	0.004	0.005	PBS*	[77]
	1.38	0.74	-343.5	0.002	0.002	PH = 7.5	
WE43	0	70	-1630	21.3	–	0.9% NaCl solution	[68]
	1.02	0.61	-1686	29.8	–		
WE43	0	61.3	-1630	21.3	–	0.9% NaCl solution	[78]
	1	0.61	-1608	30.0	–		
PT7M	0	5–10	-465	1070	–	0.2%HF + 10%HNO_3	[37]
	2.4	0.2–0.5	-483	800	–	Room temperature	

* GS: grain size; E_{corr}: corrosion potential; I_{corr}: current density; R_{corr}: corrosion rate; Ringer's solution contains 8.6 NaCl, 0.3 KCl, and 0.48 $CaCl_2$ (in gm/l); PBS containing 0.2 M NaCl + 0.1 M phosphate buffer solution.

evaluating corrosion behavior. The E_{corr} reveals thermodynamic characteristic of a metal–electrolyte system, but not the reaction kinetics of corrosion. The corrosion rate (R_{corr}) can be accurately determined from I_{corr}, which represents the total amount of corroded metal per unit time [76].

After RS process, Al alloys [61,62] and stainless steel [63,77] show significant improvement in corrosion resistance. The R_{corr} of RSed materials is only half that of the corresponding CG counterpart before deformation. Obviously, the RSed UFG microstructure has better corrosion resistance. Al and stainless steel (SS) tend to form a passivation film in sodium chloride solution or simulating human body fluid. This passivation film separates the collective from the corrosive medium to prevent further corrosion. Compared to CG, the UFG materials have a high density of GBs which are the short-circuiting channels for the outward diffusion of atoms in the material. Therefore, the UFG Al and SS form passivation film fast and maintains the stability of this film. Observing the corrosion results of copper in Hank's solution, it can be found that the corrosion resistance of RSed copper changes with strain, decreasing first and then increasing later. When strain is small, the increased dislocation density and higher stored strain energy act as a driving force for corrosion. When strain is high, high density of GBs facilitates the formation of a homogeneous Cu_2O due to the migration of dissolved Cu^{2+} from GBs to the grain interior. These Cu^{2+} interrupt the supply of the oxidizer resulting in a decrease in cathodic current and hence the R_{corr} [76].

However, when the WE43 alloy (a Mg alloy) is in 0.9% NaCl solution, the RSed UFG microstructure does not lead to deterioration of the resistance to electrochemical and chemical corrosion, as shown in Table 2. The similar result is also obtained by measuring the mass loss and the volume of evolved hydrogen [78]. Martynenko et al. suggested that the corrosion resistance of UFG WE43 alloy is influenced by two reasons: (1) an increase in the density of dislocations leads to a reduction of the corrosion resistance, (2) UFG structure enhances the formation of a protective surface layer consisting of MgO and MgOH [68].

3.2.5. Electrical conductivity

As a good conductor of electricity, metallic materials such as silver, copper and aluminum are widely used in electrical engineering and electronic components [79]. Considering only the microstructure, all the factors that cause distortion in the metal matrix (impurity/solute elements, vacancies, GBs, dislocations, phase boundaries, etc.) increase the scattering of electrons, which manifests itself macroscopically as high resistance. However, the strengthening of the metal is strongly dependent on these defects. Thus, the strength-conductivity paradox appears.

The RSed Cu with a strain of 2.5 has a fractal-like microstructure which has been proved to be a structure with enhanced electron transport efficiency [39]. Fig. 12 schematically illustrates microstructural evolutions of Cu during RS and subsequent annealing

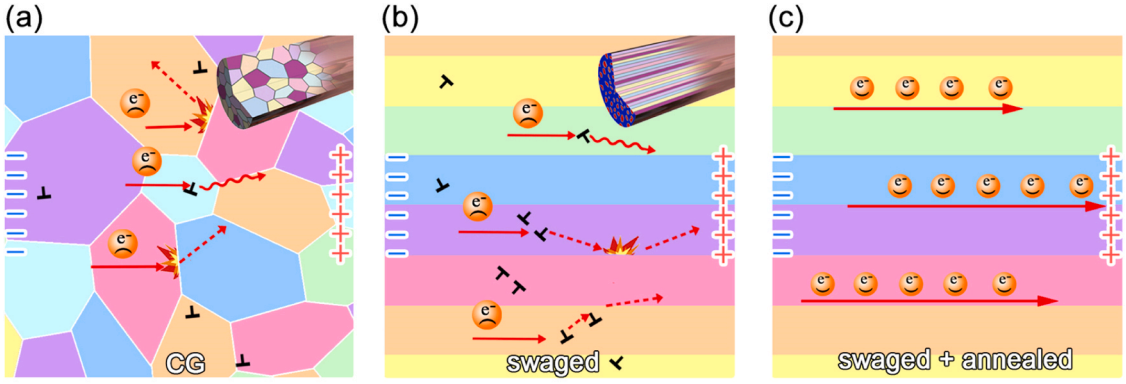

Fig. 12. Schematic representation of microstructural evolutions of pure Cu during swaging and annealing processes and their influences on electrical conductivity. (a) coarse grain, CG; (b) rotary swaged pure Cu; (c) rotary swaged + annealed [39].
Reproduced with permission from Ref. [39].

processes and their influences on the conductive properties. The electrons are driven by the applied electric potential and move in the axial direction (indicated by plus and minus). In the case of CG Cu, high-angle GBs and free dislocations are the main lattice imperfections that influence electrical conductivity, the electrical conductivity is ~100% IACS (International Annealed Copper Standard) at this point, as shown in Fig. 12(a). After RS, the grains elongation along the axial direction, a large number of dislocations are introduced, the electrical conductivity down to ~97% IACS (Fig. 12(b)). Subsequent annealing prior to recrystallization removes most of the dislocations on the electron channels, reduces electron scattering and enhances the conductivity to ~103% IACS, as shown in Fig. 12(c).

4. Outlook

The RS is a traditional metal deformation process, and in the last decade the focus has shifted from equipment development to product performance, such as material strengthening through the preparation of UFG microstructure. However, the research on the RSed materials is still niche compared to other SPD methods. Several future issues need to be studied in RS:

(1) Current research has focused on the cold (room temperature) and hot RS, and the deformation mechanism and properties of the material during RS at low temperature (such as liquid nitrogen) are yet to be studied;
(2) Gradient structure can be introduced to materials by RS, and the quantitative correspondence between RS-processed gradient structure and properties need to be established;
(3) The distribution, property and impact of residual stress should be studied;
(4) Fatigue and corrosion behavior and associated failure mechanisms of the RSed materials should be systematically examined in an effort to explore its engineering applications;
(5) Non-rotary bars, such as eight prism, can be obtained by means of RS [80,81] and it appears that clever mechanical design is required to produce bars with more complex cross-sections.

5. Conclusions

In this paper, we first review the principle and unique characteristics of RS, then compare the advantages and disadvantages of RS and other SPD methods, and systematically summarized the microstructural characteristics, mechanical properties, physical and chemical properties of various UFG metals prepared by RS. The UFG microstructure was successfully introduced to various bulk metallic materials with large dimensions by means of an industrial technique of RS, thanks to the complex stresses throughout the material. Moreover, RSed UFG metals usually have been proven to have superior properties, including micro-hardness, conductivity, corrosion, etc.

Funding

This research was funded by the National Natural Science Foundation of China (Grant No. 51971112, 51225102 and 11922211), National Key Research and Development Program of China (Grant No. 2017YFA0204403) and the Fundamental Research Funds for the Central Universities (No. 30919011405).

CRediT authorship contribution statement

Qingzhong Mao: Conceptualization, Data curation, Writing – original draft. **Yanfang Liu:** Data curation, Writing – original draft. **Yonghao Zhao:** Conceptualization, Writing – review & editing, Funding acquisition. All authors have read and approved the article for publication.

Declaration of competing Interest

The authors declare that they have no known competing financial interests or personal relationships that could have appeared to influence the work reported in this paper.

References

[1] Y.H. Zhao, J.F. Bingert, X.Z. Liao, B.Z. Cui, K. Han, A.V. Sergueeva, A.K. Mukherjee, R.Z. Valiev, T.G. Langdon, Y.T. Zhu, Simultaneously increasing the ductility and strength of ultra-fine-grained pure copper, Adv. Mater. 18 (2006) 2949–2953.
[2] Y. Zhu, K. Ameyama, P.M. Anderson, I.J. Beyerlein, H. Gao, H.S. Kim, E. Lavernia, S. Mathaudhu, H. Mughrabi, R.O. Ritchie, N. Tsuji, X. Zhang, X. Wu, Heterostructured materials: superior properties from hetero-zone interaction, Mater. Res. Lett. 9 (2021) 1–31.
[3] D. Mattissen, D. Raabe, F. Heringhaus, Experimental investigation and modeling of the influence of microstructure on the resistive conductivity of a Cu–Ag–Nb in situ composite, Acta Mater. 47 (1999) 1627–1634.
[4] E.O. Hall, The deformation and ageing of mild steel: III Discussion of results, Proc. Phys. Soc. B 64 (1951) 747–753.
[5] N.J. Petch, The cleavage strength of polycrystals, J. Iron Steel Inst. 174 (1953) 25–28.
[6] Z. Shan, E.A. Stach, J.M. Wiezorek, J.A. Knapp, D.M. Follstaedt, S.X. Mao, Grain boundary-mediated plasticity in nanocrystalline nickel, Science 305 (2004) 654–657.
[7] T.J. Rupert, D.S. Gianola, Y. Gan, K.J. Hemker, Experimental observations of stress-driven grain boundary migration, Science 326 (2009) 1686–1690.
[8] J. Hu, Y.N. Shi, X. Sauvage, G. Sha, K. Lu, Grain boundary stability governs hardening and softening in extremely fine nanograined metals, Science 355 (2017) 1292–1296.
[9] M.A. Meyers, A. Mishra, D.J. Benson, Mechanical properties of nanocrystalline materials, Prog. Mater. Sci. 51 (2006) 427–556.
[10] J. Li, Q. Mao, M. Chen, W. Qin, X. Lu, T. Liu, D. She, J. Kang, G. Wang, X. Zhu, Y. Li, Enhanced pitting resistance through designing a high-strength 316L stainless steel with heterostructure, J. Mater. Res. Technol. 10 (2021) 132–137.
[11] W. Qin, J. Li, Y. Liu, W. Yue, C. Wang, Q. Mao, Y. Li, Effect of rolling strain on the mechanical and tribological properties of 316 L stainless steel, J. Tribol. 141 (2019) 021606.
[12] Y. Liu, F. Wang, Y. Cao, J. Nie, H. Zhou, H. Yang, X. Liu, X. An, X. Liao, Y. Zhao, Y. Zhu, Unique defect evolution during the plastic deformation of a metal matrix composite, Scr. Mater. 162 (2019) 316–320.
[13] Y. Liu, Y. Cao, Q. Mao, H. Zhou, Y. Zhao, W. Jiang, Y. Liu, J.T. Wang, Z. You, Y. Zhu, Critical microstructures and defects in heterostructured materials and their effects on mechanical properties, Acta Mater. 189 (2020) 129–144.
[14] Y. Chen, J. Nie, F. Wang, H. Yang, C. Wu, X. Liu, Y. Zhao, Revealing hetero-deformation induced (HDI) stress strengthening effect in laminated Al-(TiB2+TiC) p/6063 composites prepared by accumulative roll bonding, J. Alloy. Compd. 815 (2020) 152285.
[15] T. Hebesberger, H.P. Stüwe, A. Vorhauer, F. Wetscher, R. Pippan, Structure of Cu deformed by high pressure torsion, Acta Mater. 53 (2005) 393–402.
[16] Y. Wei, Y. Li, L. Zhu, Y. Liu, X. Lei, G. Wang, Y. Wu, Z. Mi, J. Liu, H. Wang, H. Gao, Evading the strength-ductility trade-off dilemma in steel through gradient hierarchical nanotwins, Nat. Commun. 5 (2014) 3580.
[17] L. Lu, X. Chen, X. Huang, K. Lu, Revealing the maximum strength in nanotwinned copper, Science 323 (2009) 607–610.
[18] L. Lu, Y. Shen, X. Chen, L. Qian, K. Lu, Ultrahigh strength and high electrical conductivity in copper, Science 304 (2004) 422–426.
[19] K. Mertova, J. Palan, M. Duchek, T. Studecky, J. Dzugan, I. Polakova, Continuous Production of pure titanium with ultrafine to nanocrystalline microstructure, Materials 13 (2020) 336.
[20] S. Giribaskar, Gouthama, R. Prasad, Ultra-fine grained Al-SiC metal matrix composite by rotary swaging process, Mater. Sci. Forum 702–703 (2012) 320–323.
[21] J. Li, Y. Cao, B. Gao, Y. Li, Y. Zhu, Superior strength and ductility of 316L stainless steel with heterogeneous lamella structure, J. Mater. Sci. 53 (2018) 10442–10456.
[22] Q. Mao, X. Chen, J. Li, Y. Zhao, Nano-gradient materials prepared by rotary swaging, Nanomaterials 11 (2021) 2223.
[23] S.J. Lim, H.J. Choi, K.H. Na, C.H. Lee, Dimensional characteristics of products using rotary swaging machine with four-dies, Solid State Phenom. 124–126 (2007) 1645–1648.
[24] V. Piwek, B. Kuhfuss, E. Moumi, M. Hork, Light weight design of rotary swaged components and optimization of the swaging process, Int. J. Mater. Form. 3 (2010) 845–848.
[25] G. Singh, B. Kalita, K.I. Vishnu Narayanan, U.K. Arora, M.M. Mahapatra, R. Jayaganthan, Finite element analysis and experimental evaluation of residual stress of Zr-4 alloys processed through swaging, Metals 10 (2020) 1281.
[26] Q.L. Hao, J.T. Han, J.J. Song, S. Ji, Causes and remedies for some physical defects in rotary swaged products, Adv. Mater. Res. 941–944 (2014) 1797–1801.
[27] L. Rong, Z.R. Nie, T.Y. Zuo, FEA modeling of effect of axial feeding velocity on strain field of rotary swaging process of pure magnesium, Trans. Nonferrous Met. Soc. China 16 (2006) 1015–1020.
[28] A. Meng, X. Chen, J. Nie, L. Gu, Q. Mao, Y. Zhao, Microstructure evolution and mechanical properties of commercial pure titanium subjected to rotary swaging, J. Alloy. Compd. 859 (2021) 158222.

[29] Y. Yang, J. Nie, Q. Mao, Y. Zhao, Improving the combination of electrical conductivity and tensile strength of Al 1070 by rotary swaging deformation, Results Phys. 13 (2019) 102236.
[30] W. Pachla, M. Kulczyk, S. Przybysz, J. Skiba, K. Wojciechowski, M. Przybysz, K. Topolski, A. Sobolewski, M. Charkiewicz, Effect of severe plastic deformation realized by hydrostatic extrusion and rotary swaging on the properties of CP Ti grade 2, J. Mater. Process. Technol. 221 (2015) 255–268.
[31] F. Otto, J. Frenzel, G. Eggeler, On the influence of small quantities of Bi and Sb on the evolution of microstructure during swaging and heat treatments in copper, J. Alloy. Compd. 509 (2011) 4073–4080.
[32] R. Kocich, L. Kunčická, P. Král, P. Strunz, Characterization of innovative rotary swaged Cu-Al clad composite wire conductors, Mater. Des. 160 (2018) 828–835.
[33] S. Kuramoto, T. Furuta, Severe plastic deformation to achieve high strength and high ductility in Fe–Ni based alloys with lattice softening, Mater. Trans. 60 (2019) 1116–1122.
[34] L. Kunčická, R. Kocich, C. Hervoches, A. Macháčková, Study of structure and residual stresses in cold rotary swaged tungsten heavy alloy, Mater. Sci. Eng., A 704 (2017) 25–31.
[35] D. Canelo-Yubero, R. Kocich, C. Hervoches, P. Strunz, L. Kunčická, L. Krátká, Neutron diffraction study of residual stresses in a W–Ni–Co heavy alloy processed by rotary swaging at room and high temperatures, Met. Mater. Int. (2021).
[36] P. Strunz, R. Kocich, D. Canelo-Yubero, A. Machackova, P. Beran, L. Kratka, Texture and differential stress development in W/Ni-Co composite after rotary swaging, Materials 13 (2020) 2869.
[37] V.N. Chuvil'deev, V.I. Kopylov, A.V. Nokhrin, P.V. Tryaev, N.Y. Tabachkova, M.K. Chegurov, N.A. Kozlova, A.S. Mikhaylov, A.V. Ershova, M.Y. Grayznov, I.S. Shadrina, C.V. Likhnitskii, Effect of severe plastic deformation realized by rotary swaging on the mechanical properties and corrosion resistance of near-α-titanium alloy Ti-2.5Al-2.6Zr, J. Alloy. Compd. 785 (2019) 1233–1244.
[38] Q. Mao, Y. Zhang, Y. Guo, Y. Zhao, Enhanced electrical conductivity and mechanical properties in thermally stable fine-grained copper wire, Commun. Mater. 2 (2021) 46.
[39] Q. Mao, Y. Zhang, J. Liu, Y. Zhao, Breaking material property trade-offs via macrodesign of microstructure, Nano Lett. 21 (2021) 3191–3197.
[40] S.J. Park, S. Muraishi, Influence of residual stress around constituent particles on recrystallization and grain growth in Al-Mn-based alloy during annealing, Materials 14 (2021) 1701.
[41] E. Moumi, S. Ishkina, B. Kuhfuss, T. Hochrainer, A. Struss, M. Hunkel, 2D-simulation of material flow during infeed rotary swaging using finite element method, Procedia Eng. 81 (2014) 2342–2347.
[42] A. Machackova, L. Kratka, R. Petrmichl, L. Kuncicka, R. Kocich, Affecting structure characteristics of rotary swaged tungsten heavy alloy via variable deformation temperature, Materials 12 (2019) 4200.
[43] Y. Cao, S. Ni, X. Liao, M. Song, Y. Zhu, Structural evolutions of metallic materials processed by severe plastic deformation, Mater. Sci. Eng., R 133 (2018) 1–59.
[44] J. Čubrová, K. Mertová, M. Duchek, Effects of rotary swaging, wire drawing and their combination on the resulting properties of nickel-alloy wires, Mater. Tehnol. 54 (2020) 601–606.
[45] A.H. Huang, Y.F. Wang, M.S. Wang, L.Y. Song, Y.S. Li, L. Gao, C.X. Huang, Y.T. Zhu, Optimizing the strength, ductility and electrical conductivity of a Cu-Cr-Zr alloy by rotary swaging and aging treatment, Mater. Sci. Eng., A 746 (2019) 211–216.
[46] Z.W. Huang, S.B. Jin, H. Zhou, Y.S. Li, Y. Cao, Y.T. Zhu, Evolution of twinning systems and variants during sequential twinning in cryo-rolled titanium, Int. J. Plast. 112 (2019) 52–67.
[47] Z.W. Huang, P.L. Yong, N.N. Liang, Y.S. Li, Slip, twinning and twin-twin interaction in a gradient structured titanium, Mater. Charact. 149 (2019) 52–62.
[48] K. Wei, R. Hu, D. Yin, L. Xiao, S. Pang, Y. Cao, H. Zhou, Y. Zhao, Y. Zhu, Grain size effect on tensile properties and slip systems of pure magnesium, Acta Mater. 206 (2021) 116604.
[49] X. Luo, Z. Feng, T. Yu, J. Luo, T. Huang, G. Wu, N. Hansen, X. Huang, Transitions in mechanical behavior and in deformation mechanisms enhance the strength and ductility of Mg-3Gd, Acta Mater. 183 (2020) 398–407.
[50] J.L. Sun, P.W. Trimby, F.K. Yan, X.Z. Liao, N.R. Tao, J.T. Wang, Grain size effect on deformation twinning propensity in ultrafine-grained hexagonal close-packed titanium, Scr. Mater. 69 (2013) 428–431.
[51] M. Wang, Y. Wang, A. Huang, L. Gao, Y. Li, C. Huang, Promising tensile and fatigue properties of commercially pure titanium processed by rotary swaging and annealing treatment, Materials 11 (2018) 2261.
[52] Y. Yang, X. Chen, J. Nie, K. Wei, Q. Mao, F. Lu, Y. Zhao, Achieving ultra-strong magnesium–lithium alloys by low-strain rotary swaging, Mater. Res. Lett. 9 (2021) 255–262.
[53] Y. Wan, B. Tang, Y. Gao, L. Tang, G. Sha, B. Zhang, N. Liang, C. Liu, S. Jiang, Z. Chen, X. Guo, Y. Zhao, Bulk nanocrystalline high-strength magnesium alloys prepared via rotary swaging, Acta Mater. 200 (2020) 274–286.
[54] X. Chen, C. Liu, Y. Wan, S. Jiang, Z. Chen, Y. Zhao, Grain refinement mechanisms in gradient nanostructured AZ31B Mg alloy prepared via rotary swaging, Metall. Mater. Trans. A 52 (2021) 4053–4065.
[55] E. Knauer, J. Freudenberger, T. Marr, A. Kauffmann, L. Schultz, Grain refinement and deformation mechanisms in room temperature severe plastic deformed Mg-AZ31, Metals 3 (2013) 283–297.
[56] R. Kocich, L. Kunčická, D. Dohnalík, A. Macháčková, M. Šofer, Cold rotary swaging of a tungsten heavy alloy: numerical and experimental investigations, Int. J. Refract. Met. Hard Mater. 61 (2016) 264–272.
[57] G.R. Goren-Muginstein, A. Rosen, The effect of cold deformation on grain refinement of heavy metals, Mater. Sci. Eng., A 238 (1997) 351–356.
[58] X. Yang, H. Tan, N. Lin, Z. Li, Y. He, Effects of the lanthanum content on the microstructure and properties of the molybdenum alloy, Int. J. Refract. Met. Hard Mater. 61 (2016) 179–184.
[59] J. Svoboda, L. Kuncicka, N. Luptakova, A. Weiser, P. Dymacek, Fundamental improvement of creep resistance of new-generation nano-oxide strengthened alloys via hot rotary swaging consolidation, Materials 13 (2020) 5217.
[60] M.A. Abdulstaar, M. Mhaede, M. Wollmann, L. Wagner, Fatigue behaviour of commercially pure aluminium processed by rotary swaging, J. Mater. Sci. 49 (2014) 1138–1143.
[61] M. Abdulstaar, M. Mhaede, L. Wagner, M. Wollmann, Corrosion behaviour of Al 1050 severely deformed by rotary swaging, Mater. Des. 57 (2014) 325–329.
[62] M. Abdulstaar, M. Mhaede, M. Wollmann, L. Wagner, Investigating the effects of bulk and surface severe plastic deformation on the fatigue, corrosion behaviour and corrosion fatigue of AA5083, Surf. Coat. Technol. 254 (2014) 244–251.
[63] A.A. Ahmed, M. Mhaede, M. Wollmann, L. Wagner, Effect of surface and bulk plastic deformations on the corrosion resistance and corrosion fatigue performance of AISI 316L, Surf. Coat. Technol. 259 (2014) 448–455.
[64] M. Droste, C. Ullrich, M. Motylenko, M. Fleischer, A. Weidner, J. Freudenberger, D. Rafaja, H. Biermann, Fatigue behavior of an ultrafine-grained metastable CrMnNi steel tested under total strain control, Int. J. Fatigue 106 (2018) 143–152.
[65] A.A. Tokar, V.A. Lunev, A.S. Dolzhenko, O.V. Rybalchenko, M.M. Morozov, V.S. Yusupov, G.V. Rybalchenko, P.D. Odessky, S.V. Dobatkin, Effect of rotary swaging on structure and properties of low-carbon steel, IOP Conf. Ser.: Mater. Sci. Eng. 848 (2020).
[66] H. Alkhazraji, E. El-Danaf, M. Wollmann, L. Wagner, Enhanced fatigue strength of commercially pure ti processed by rotary swaging, Adv. Mater. Sci. Eng. 2015 (2015) 1–12.
[67] I.M. Modina, V.V. Polyakova, G.S. Dyakonov, A.V. Polyakov, I.P. Semenova, A.G. Raab, Mechanical behavior and impact toughness of the ultrafine-grained VT8M-1 alloy, IOP Conf. Ser.: Mater. Sci. Eng. 672 (2019) 012044.
[68] S.V. Dobatkin, E.A. Lukyanova, N.S. Martynenko, N.Y. Anisimova, M.V. Kiselevskiy, M.V. Gorshenkov, N.Y. Yurchenko, G.I. Raab, V.S. Yusupov, N. Birbilis, G.A. Salishchev, Y.Z. Estrin, Strength, corrosion resistance, and biocompatibility of ultrafine-grained Mg alloys after different modes of severe plastic deformation, IOP Conf. Ser.: Mater. Sci. Eng. 194 (2017) 012004.
[69] N. Durlu, N.K. Çalişkan, Ş. Bor, Effect of swaging on microstructure and tensile properties of W–Ni–Fe alloys, Int. J. Refract. Met. Hard Mater. 42 (2014) 126–131.
[70] M.F. Hupalo, A.F. Padilha, H.R.Z. Sandim, A.M. Kliauga, Cold Swaging, Recovery and recrystallization of oligocrystalline INCOLOY MA 956-Part I: deformed state, ISIJ Int. 44 (2004) 1894–1901.
[71] D. Garcia Borges, M.R. Baldissera, G. Rodrigues, Md.L.N.M. Melo, R.F. Ribeiro Lourenço, G. Silva, Microstructural and mechanical characterization of the niobium cold deformed-swage, Mater. Sci. Forum 805 (2014) 362–367.
[72] M.J. Starink, S.C. Wang, A model for the yield strength of overaged Al–Zn–Mg–Cu alloys, Acta Mater. 51 (2003) 5131–5150.
[73] G. Laplanche, O. Horst, F. Otto, G. Eggeler, E.P. George, Microstructural evolution of a CoCrFeMnNi high-entropy alloy after swaging and annealing, J. Alloy. Compd. 647 (2015) 548–557.
[74] A. Klumpp, S. Maier, H. Chen, M. Fotouhi, R. Schneider, S. Dietrich, K.-H. Lang, V. Schulze, Influence of work-hardening on fatigue crack growth, effective threshold and crack opening behavior in the nickel-based superalloy Inconel 718, Int. J. Fatigue 116 (2018) 257–267.
[75] Y. Kimura, T. Inoue, F. Yin, K. Tsuzaki, Inverse temperature dependence of toughness in an ultrafine grain-structure steel, Science 320 (2008) 1057–1060.
[76] M. Gholami, M. Mhaede, F. Pastorek, I. Altenberger, B. Hadzima, M. Wollmann, L. Wagner, Corrosion behavior and mechanical properties of ultrafine-grained pure copper with potential as a biomaterial, Adv. Eng. Mater. 18 (2016) 615–623.
[77] I. Bösing, M. Herrmann, I. Bobrov, J. Thöming, B. Kuhfuss, J. Epp, M. Baune, The influence of microstructure deformation on the corrosion resistance of cold formed stainless steel, MATEC Web Conf. 190 (2018) 01002.
[78] N. Martynenko, E. Lukyanova, M. Gorshenkov, M. Morozov, V. Yusupov, N. Birbilis, S. Dobatkin, Y. Estrin, Strengthening of magnesium alloy WE43 by rotary swaging, Mater. Sci. Forum 941 (2018) 808–813.
[79] H. Yang, Z. Ma, C. Lei, L. Meng, Y. Fang, J. Liu, H. Wang, High strength and high conductivity Cu alloys: a review, Sci. China.: Technol. Sci. 63 (2020) 2505–2517.
[80] L. Rong, Z. Nie, T. Zuo, 3D finite element modeling of cogging-down rotary swaging of pure magnesium square billet—revealing the effect of high-frequency pulse stroking, Mater. Sci. Eng., A 464 (2007) 28–37.
[81] S. Ishkina, B. Kuhfuss, C. Schenck, Grain size modification by micro rotary swaging, Key Eng. Mater. 651–653 (2015) 627–632.